Quartet structure generation set algorithm based 3D reconstruction on porous structures of sintered copper joints for power electronics packaging

Liu, Wenting; Wang, Xinyue; Zhang, Jing; Zhang, Guoqi; Chen, Chuantong; Liu, Pan

DOI
10.1016/j.scriptamat.2025.116750

Publication date
2025

Document Version
Final published version

Published in
Scripta Materialia

Citation (APA)
Liu, W., Wang, X., Zhang, J., Zhang, G., Chen, C., & Liu, P. (2025). Quartet structure generation set algorithm based 3D reconstruction on porous structures of sintered copper joints for power electronics packaging. *Scripta Materialia*, *265*, Article 116750. https://doi.org/10.1016/j.scriptamat.2025.116750

Scripta Materialia 265 (2025) 116750

Contents lists available at ScienceDirect

Scripta Materialia

journal homepage: www.journals.elsevier.com/scripta-materialia

Quartet structure generation set algorithm based 3D reconstruction on porous structures of sintered copper joints for power electronics packaging

Wenting Liu [a], Xinyue Wang [a], Jing Zhang [b], Guoqi Zhang [c], Chuantong Chen [d], Pan Liu [a,e,*]

[a] Academy for Engineering & Technology, Fudan University, Shanghai 200433, China
[b] Heraeus Materials Technology Shanghai Ltd., Shanghai 201108, China
[c] Department of Microelectronics, Delft University of Technology, 2628 CD, Delft, the Netherlands
[d] Flexible 3D System Integration Laboratory, Osaka University, Osaka 565-0871, Japan
[e] Research Institute of Fudan University in Ningbo, Zhejiang Province 315336, China

ARTICLE INFO

Keywords:
Sintering
Porous material
3D reconstruction
Finite element analysis
Performance

ABSTRACT

Sintered materials have been widely applied, as an alternative to soldering, for power electronics packaging. One key issue for such die-attach material is to characterize the actual porosity, which is difficult to obtain through SEM cross-section analysis. Therefore, in this work, the optimized Quartet Structure Generation Set (QSGS) algorithm was applied to sintered copper joints under various porosity levels to reconstruct 3D porous structures based on 2D SEM images. Firstly, copper joints with varying porosities were fabricated under different sintering conditions. Reconstructed 3D porous copper models were then generated through the QSGS algorithm to match experimental observations, including porosity and pore size. Finite element analysis (FEA) simulations were further conducted to explore the effects of pores on thermal and electrical performance. This work provides a method for accurately predicting the thermoelectric properties of sintered copper joints and insights for optimizing copper sintering in power electronics applications.

With the development of wide-bandgap semiconductor materials such as SiC and GaN, power devices are facing harsher operation environments, including larger current capacities, higher voltages, and elevated working temperatures [1–3]. To meet these demands, sintering has emerged as a novel die-attach technology, offering superior thermal and electrical performance [4–7]. In recent years, copper sintering has gained increasing attention for die-attach applications as a cost-effective alternative, delivering thermal and electrical performance comparable to silver [8–10].

One distinctive feature of such sintered copper joints is their porous structure, which arises from the evaporation of organic solvents and the volume shrinkage of copper particles during densification [11,12]. These air-filled pores significantly affect the overall performance of the joints, influencing both their thermal and electrical properties [13,14]. Therefore, understanding the role of pores in heat and current transport is critical for optimizing the performance of sintered copper joints in practical applications. However, most existing studies focus on the process parameters and material compositions for the porosity of sintered copper, limited attention is addressed for the quantitative relationship between porosity, pore size, and joint performance [15–20]. Meanwhile, the characterization of pore structures has mainly focused on 2D analysis, and a more convenient and accurate method for 3D structural analysis is needed.

In this study, copper joints with three different porosity levels were first fabricated and characterized by cross-sectional Scanning Electron Microscope (SEM). Subsequently, the Quartet Structure Generation Set (QSGS) algorithm proposed by Wang et al. [21]. was optimized and applied to 2D SEM images to reconstruct 3D porous copper models matching the experimental pore features. Afterward, finite element simulations were performed on the reconstructed models to predict their thermal and electrical performance. Finally, the simulation results were compared with the experimental measurements, and the model was further refined accordingly. This approach not only revealed the relationship between pore characteristics and joint performance but also achieved a robust method for accurately predicting the thermoelectric properties of sintered copper joints.

Firstly, to fabricate sintered copper samples with varying porosities, three cylindrical specimens (1 mm thick, 12.7 mm in diameter) were prepared using copper sintering paste provided by Heraeus Shanghai Ltd. The samples were sintered using a Boschman SinterStar machine at

---

[*] Corresponding author at: Academy for Engineering & Technology, Fudan University, Shanghai 200433, China.
E-mail address: panliu@fudan.edu.cn (P. Liu).

https://doi.org/10.1016/j.scriptamat.2025.116750
Received 25 January 2025; Received in revised form 24 April 2025; Accepted 3 May 2025

250 °C under a constant pressure of 10 MPa for durations of 10, 20, and 30 min, respectively. Subsequently, cross-sectional SEM was used to characterize the microstructures of the sintered samples.

Cross-sectional images under different sintering durations revealed distinct variations in porosities and pore sizes (i.e., pore areas). As shown in Fig. 1, the average porosities for sintering durations of 10, 20, and 30 min were 30.75 %, 23.02 %, and 16.50 %, respectively, based on analysis using ImageJ. These porosity values were categorized as Porosity Levels A, B, and C. Correspondingly, average pore sizes, calculated using MATLAB (2023a), were 0.0074 μm^2, 0.0090 μm^2, and 0.0105 μm^2 . The results showed that insufficient diffusion occurred between copper particles at shorter sintering durations. This resulted in greater particle separation and a looser internal structure, leading to higher porosity and smaller pore sizes. In contrast, longer sintering durations promoted the formation of sintering necks and enhanced particle bonding. Smaller pores gradually coalesced into larger ones, resulting in more condensed sintered structures. Thus, at a sintering duration of 30 min, the sintered joints exhibited the lowest average porosity and the largest average pore size.

Secondly, the QSGS algorithm was employed to generate 3D models of sintered copper with random pore distributions, owing to its high accuracy in representing actual porous structures. The algorithm was refined to establish models with pore features closely matching SEM cross-section observations, including porosity and pore size obtained from previous experimental results.

In the reconstruction process, considering particle volume shrinkage and pore growth during the sintering process, the initial matrix was assumed to be the pure solid phase, while the porous phase was considered to be the growing phase. The reconstruction process can be divided into the following steps, as shown in Fig. 2:

(1) Input initial reconstruction parameters: define the model dimensions (l_x, l_y, l_z), the initial directional growth probabilities (D_i), the pore seed probability (C_{dd}), and the initial volume porosity ($P_{3d\text{-}sim}$).
(2) Input target 2D porosity and pore size: define the target mean porosity ($P_{2d\text{-}target}$) and mean pore size($A_{2d\text{-}target}$) based on three SEM images.
(3) Perform reconstruction and filter optimization: A number of pore seeds are randomly generated based on the seed distribution probability C_{dd}. Then, these seeds grow into neighboring cells in all directions. Each neighboring cell is assigned a random number between 0 and 1. If the number is less than the corresponding directional growth probability D_i, the cell is “occupied” by the growing pore phase. This process continues until the target volume porosity $P_{3d\text{-}sim}$ is reached. To improve structural quality, a kernel-based noise filter is applied to smooth the edges of the generated pores.
(4) Slice and analyze the reconstructed model: the reconstructed 3D model is sliced into ten uniform 2D layers along the y-direction to match the angle in practical SEM observations. Then, calculate the mean porosity and mean pore size for each slice.
(5) Compare simulated results with experimental data: calculate the average simulated 2D porosity ($P_{2d\text{-}sim}$) and pore size ($A_{2d\text{-}sim}$) of the ten sliced 2D layers and compare them with the experimentally obtained values ($P_{2d\text{-}target}$ and $A_{2d\text{-}target}$) from SEM images. Check whether the error is within 5 %. If the error is not within 5 %, return to step (1) to adjust reconstruction parameters. If the error is within 5 %, proceed to step (6).
(6) Output the final porous reconstruction model: generate the final 3D reconstruction model and output the results, including $P_{3d\text{-}sim}$, $P_{2d\text{-}sim}$, and $A_{2d\text{-}sim}$, to validate the reconstruction.

Based on such a reconstruction process, 3D porous models were established in MATLAB (2023a) to investigate the pore effects on the thermal/electrical performance of sintered copper joints. Each model was constructed with a size of 40 × 40 × 40 voxels. The scaling ratio between the actual dimensions and the simulation model was set as $1{:}\sqrt{10}$, implying that the actual pore areas obtained from the SEM images were magnified tenfold to reconstruct the 3D porous model.

Thirdly, FEM simulations were conducted based on the established 3D reconstruction models. The simulations focused on both thermal and electrical analysis using COMSOL Multiphysics 6.1, with the Heat Transfer and AC/DC modules, respectively. To ensure a uniform distribution of heat and current inputs, two thin copper layers were added to the top and bottom of the model to mitigate the edge effects caused by

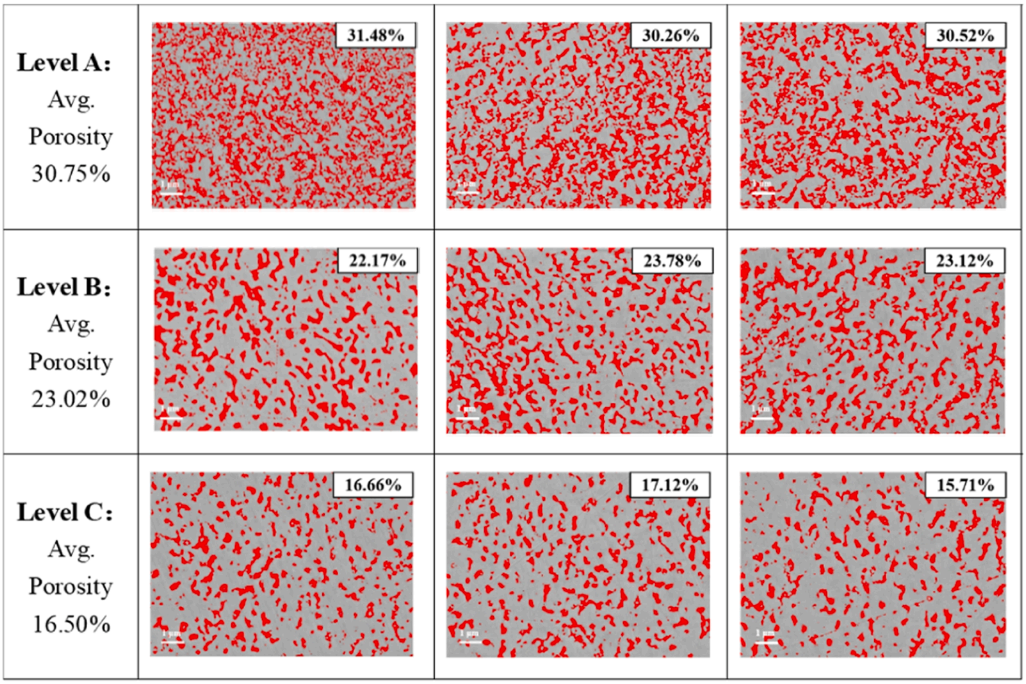

Fig. 1. Cross-sectional SEM images of sintered copper joints with varying porosity levels.

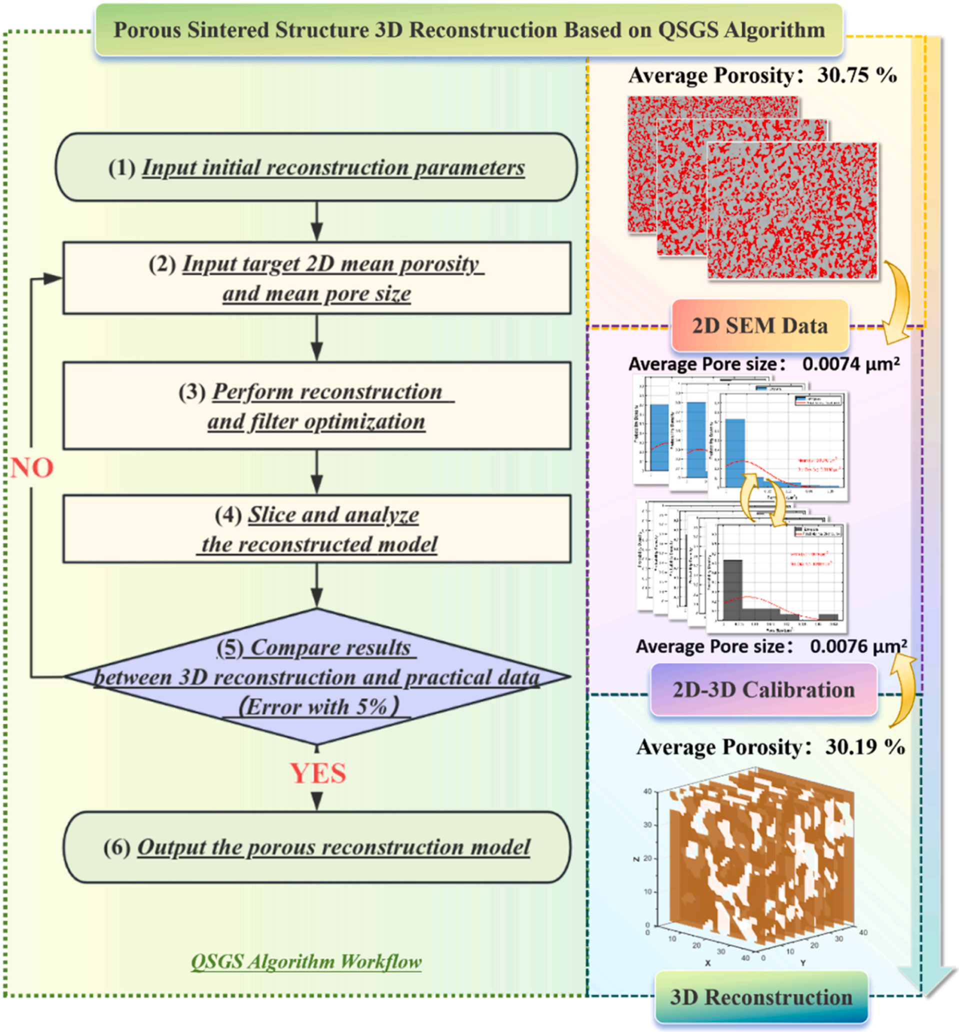

Fig. 2. Illustration of the workflow for 3D reconstruction of sintered porous structures.

surface pores. These layers were subsequently removed in the analysis to focus on the intrinsic properties of the porous regions. Thermal and electrical insulation conditions were applied to the pore boundaries and the other surfaces of the models. An adaptive meshing method using the standard setting in COMSOL was applied to improve accuracy near regions with sharp gradients.

For the thermal simulations, a heat flux density of 1 W/mm^2 was applied to the top surface (hot end), while the bottom surface was maintained at a fixed temperature of 293.15 K (cold end). The thermal conductivities of the porous models were calculated using Fourier's law, as shown in Eq. (1):

$$q = -k\frac{dT}{dz} \tag{1}$$

where q is the heat flux density, k is the thermal conductivity, dT is the temperature difference, and dz is the heat transfer distance.

For the electrical simulations, a current density of 1 A/m^2 was injected through the top surface, while the bottom surface was grounded. The electrical conductivities of the models were calculated using Eq. (2):

$$J = \sigma E = \sigma\frac{dU}{dz} \tag{2}$$

where the J is the current density, σ is the electrical conductivity, E is the electrical field, dU is the potential difference, and dz is the current transfer distance.

During the FEM simulation analysis, different pore locations and porosity levels were considered.

Firstly, to analyze the influence of pore location, the QSGS stochastic algorithm was used to generate three different sintered structures for joint performance analysis under the same porosity level (i.e., Porosity Level B). Fig. 3 presents the simulated temperature and electrical potential distributions, along with the calculated results for each model. It revealed that under the same porosity level but different stochastic pore distributions, the simulated thermal conductivities were 245.52 W/(m·K), 259.49 W/(m·K), and 241.93 W/(m·K), with an average value of 248.98±3.04 % W/(m·K). Similarly, the electrical conductivities were 3.68E7 S/m, 3.89E7 S/m, and 3.63E7 S/m with an average value of 3.73E7±3.02 % S/m. These results indicated that the thermal and electrical conductivities exhibited only minor fluctuations (within 5 %), suggesting that the random spatial distribution of pores has a limited effect on the thermal and electrical performance of the joints.

Subsequently, models with varying porosity levels were established to investigate heat and current conduction processes. To enhance the accuracy of the calculations, three models with randomly distributed pore locations were constructed in parallel for each porosity level. Table 1 summarizes the average temperature and electrical potential at the top and bottom interfaces, along with their respective differences. As presented, with an increase in porosity, the average temperature/electrical potential at the upper interface (heat/electrical current input side)

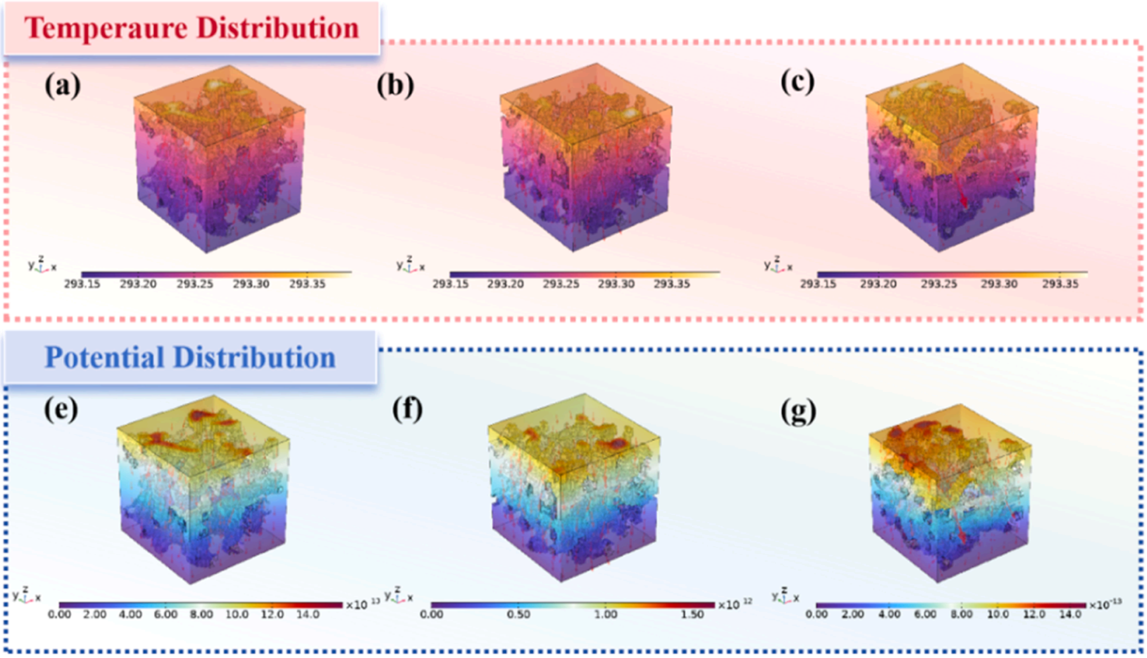

Fig. 3. Temperature and potential distribution of the reconstructed model under Porosity Level B: (a-c) temperature distribution; (e-g) potential distribution.

Table 1

Average temperature and electrical potential at the top and bottom interfaces, along with the corresponding temperature and potential differences between the two interfaces.

Porosity (Simulation)	T_{top} (K)	T_{bottom} (K)	$T_{difference}$ (K)	U_{top} (V)	U_{bottom} (V)	$U_{difference}$ (V)
Level A	293.35	293.15	0.20	1.33E-12	1.66E-15	1.32E-12
Level B	293.31	293.15	0.16	1.07E-12	1.66E-15	1.07E-12
Level C	293.27	293.15	0.12	8.18E-13	1.66E-15	8.16E-13

gradually increased, while the average temperature and electrical potential at the lower interface (cold end/grounded side) remained almost unchanged. This led to a larger temperature and electrical potential difference between the two interfaces.

Fig. 4(a-l) shows the three-dimensional spatial distributions of temperature, heat flux, electrical potential, and current density within the sintered joints. As porosity increased, the distribution of temperature and electrical potential became increasingly non-uniform, indicating that the heat transfer process within the material was significantly disrupted. Additionally, as shown in Fig. 4(d-f,j-l), both heat flux and current tended to concentrate around pores.

To more precisely quantify the relationship between porosity and thermal/electrical performance, the thermal and electrical conductivities of sintered joints at varying porosity levels were calculated using Eqs. (1) and (2), and subsequently compared with experimental data. The experimental measurements were conducted using a four-probe tester (Nuolexinda RTS-8) for electrical conductivity and a laser flash apparatus (Netzsch LFA-467) for thermal conductivity. As shown in Fig. 4(m-n), the fitting curves for both the simulated and experimental data were nearly parallel. This indicated a strong linear correlation between porosity and both thermal and electrical conductivity, with adjusted R-squared values exceeding 0.96.

However, the simulated values consistently exceeded the experimental results. This discrepancy can be attributed to idealized assumptions in the simulations, which did not account for factors such as residual organic solvents in the sintering paste, the formation of copper oxides, and other potential imperfections. These unmodeled factors may significantly influence the observed thermal/electrical properties of the joints. To bridge this gap, correction factors, including scaling (F) and offset factors (Δ_K), were introduced to adjust the simulation results for better agreement with the experimental data. The revised mathematical models are expressed as follows:

$$k_{experimental} = 1.04 * k_{simulated} - 101.55 \tag{3}$$

$$\sigma_{experimental} = 0.86 * \sigma_{simulated} - 0.63 \tag{4}$$

After calibration, these mathematical models provide a more accurate representation of the thermal and electrical conductivities. The calibrated results, shown in Table 2, were compared with the experimental results as well as the 2D-simulated results based on the QSGS calculation, demonstrating an improved accuracy in the 3D simulations. Thus, this work provides valuable insights for optimizing sintering parameters and accurately predicting the performance of sintered joints in practical applications, demonstrating the precision and effectiveness of the proposed method.

All simulations revealed that the presence of pores disrupted heat and current transport pathways within the sintered material. This effect became particularly pronounced at higher porosity levels, where the pathways available for heat and current transfer were significantly reduced. As a result, heat and current were forced through the narrow solid-phase connections, leading to localized accumulation, as illustrated in Fig. 5. In high-temperature and high-voltage environments, such localized accumulations imposed excessive stress on the already weakened solid-phase connections. These stresses may increase the risk of failure, particularly due to mismatches in the coefficient of thermal expansion between the sintered material and adjoining components.

Future research could focus on integrating advanced in situ characterization methods, such as synchrotron-based X-ray computed tomography, to dynamically monitor pore evolution during the sintering process. This approach provides insights into the time-dependent behavior of porous structures and their impact on the thermal and electrical performance of sintered materials, bridging the scientific mechanism and industrial application of porous interconnects in high-performance electronic packaging.

In conclusion, this study presented a refined QSGS algorithm,

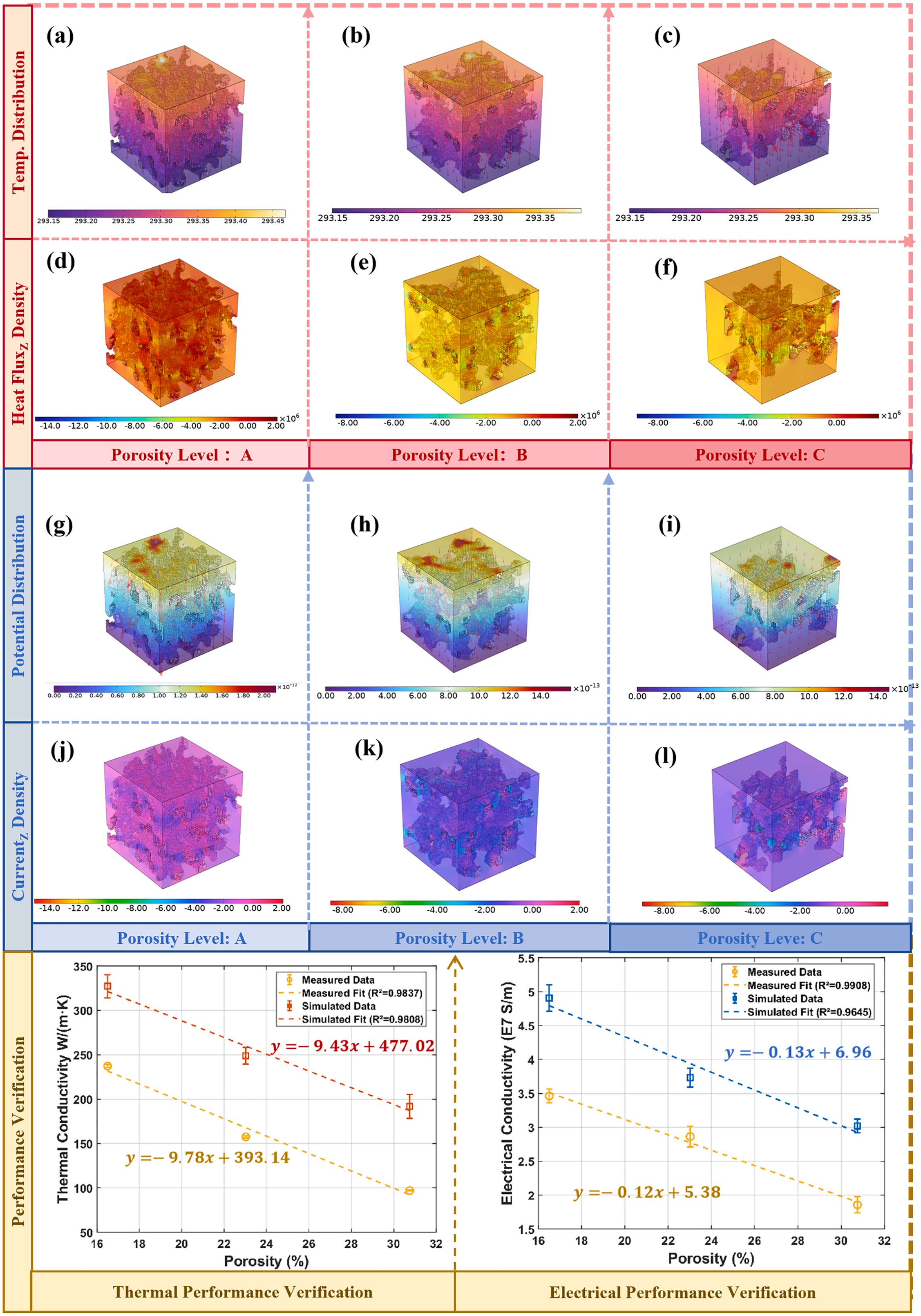

Fig. 4. FEM Simulations of porous sintered joints at different porosity levels and model verification.

Table 2
Comparison of experimental and simulated thermal and electrical conductivities at different porosity levels.

Porosity	Thermal Conductivities (W/m·K)		
	Experimental results	2D-simulated results by [11]	3D-simulated results in this work*
Level A	97.04	158.43	98.03
Level B	157.57	230.99	157.39
Level C	237.34	285.77	238.80
Porosity	**Electrical Conductivities (E7 S/m)**		
	Experimental results	2D-simulated results by [11]	3D-simulated results in this work*
Level A	1.86	2.36	1.97
Level B	2.86	3.46	2.58
Level C	3.46	4.29	3.59

* After calibration.

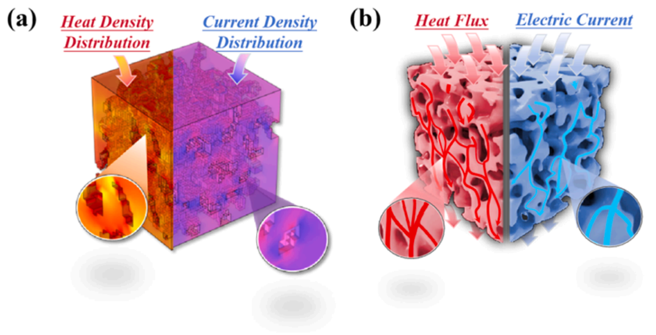

Fig. 5. Aggregation effect of heat and current in porous sintered copper joints: (a) simulated model under Porosity Level C; (b) illustration of the effect.

enhanced to reconstruct three-dimensional porous models of sintered copper that precisely reflect actual pore characteristics, such as porosity and pore size distribution. A linear relationship between the porosity and the thermal/electrical performance of sintered joints was established through finite element simulations, providing a quantitative foundation for understanding the influence of porosity on material behavior. Moreover, this study explored the mechanisms of heat flow and current aggregation within porous structures, offering valuable insights into the thermal/electrical behavior of sintered copper. By introducing correction factors to align simulated results with experimental measurements, the study demonstrated that such a method provided high-accuracy prediction of the thermal and electrical conductivities of sintered copper joints. This methodology established a robust framework for investigating and optimizing the thermal and electrical properties of porous materials, paving the way for more efficient sintering techniques in power electronics applications.

CRediT authorship contribution statement

Wenting Liu: Writing – original draft, Methodology, Formal analysis. **Xinyue Wang:** Methodology, Investigation, Data curation. **Jing Zhang:** Writing – review & editing, Supervision, Resources. **Guoqi Zhang:** Supervision. **Chuantong Chen:** . **Pan Liu:** Writing – review & editing, Supervision, Project administration, Methodology, Funding acquisition, Conceptualization.

Declaration of competing interest

The authors declare that they have no known competing financial interests or personal relationships that could have appeared to influence the work reported in this paper.

Acknowledgements

In this work, the authors would like to thank Shanghai Science & Technology Commission under Grant 24500790700, the National Natural Science Foundation of China under Grant 62304051, and Shanghai SiC Power Devices Engineering & Technology Research Center (19DZ2253400) for funding this research, providing simulation support, and laboratory access. Many thanks to Heraeus Materials Technology Shanghai Ltd. for prototype validation and characterization support, and the Chat Generative Pre-trained Transformer (ChatGPT, OpenAI) for language help.

References

[1] M. Buffolo, D. Favero, A. Marcuzzi, C.D. Santi, G. Meneghesso, E. Zanoni, M. Meneghini, Review and outlook on GaN and SiC power devices: industrial State-of-the-art, applications, and perspectives, IEEe Trans. Electron. Devices 71 (3) (2024) 1344–1355, https://doi.org/10.1109/TED.2023.3346369.

[2] F. Roccaforte, P. Fiorenza, G. Greco, R. Lo Nigro, F. Giannazzo, F. Iucolano, M. Saggio, Emerging trends in wide band gap semiconductors (SiC and GaN) technology for power devices, Microelectron. Eng. 187-188 (2018) 66–77, https://doi.org/10.1016/j.mee.2017.11.021.

[3] H. Zhang, W. Wang, H. Bai, G. Zou, L. Liu, P. Peng, W. Guo, Microstructural and mechanical evolution of silver sintering die attach for SiC power devices during high temperature applications, J. Alloys. Compd. 774 (2019) 487–494, https://doi.org/10.1016/j.jallcom.2018.10.067.

[4] Z. Zhang, C. Chen, A. Suetake, M.-C. Hsieh, A. Iwaki, K. Suganuma, Pressureless and low-temperature sinter-joining on bare Si, SiC and GaN by a Ag flake paste, Scr. Mater. 198 (2021) 113833, https://doi.org/10.1016/j.scriptamat.2021.113833.

[5] Y. Zuo, A. Robador, M. Wickham, S.H. Mannan, Unraveling the complex oxidation effect in sintered Cu nanoparticle interconnects during high temperature aging, Corros. Sci. 209 (2022) 110713, https://doi.org/10.1016/j.corsci.2022.110713.

[6] X. Liu, S. Li, J. Fan, J. Jiang, Y. Liu, H. Ye, G. Zhang, Microstructural evolution, fracture behavior and bonding mechanisms study of copper sintering on bare DBC substrate for SiC power electronics packaging, J. Mater. Res. Technol. 19 (2022) 1407–1421, https://doi.org/10.1016/j.jmrt.2022.05.122.

[7] X. Liu, H. Nishikawa, Low-pressure Cu-Cu bonding using in-situ surface-modified microscale Cu particles for power device packaging, Scr. Mater. 120 (2016) 80–84, https://doi.org/10.1016/j.scriptamat.2016.04.018.

[8] S. Lee, S.-j. Han, Y. Kim, K.-S. Jang, Copper sintering pastes with various polar solvents and acidic activators, ACS. Omega 8 (42) (2023) 39135–39142, https://doi.org/10.1021/acsomega.3c04245.

[9] S.A. McDonald, C. Holzner, E.M. Lauridsen, P. Reischig, A.P. Merkle, P.J. Withers, Microstructural evolution during sintering of copper particles studied by laboratory diffraction contrast tomography (LabDCT), Sci. Rep. 7 (1) (2017) 5251, https://doi.org/10.1038/s41598-017-04742-1.

[10] Y. Zuo, C. Zhao, A. Robador, M. Wickham, S.H. Mannan, Quasi-in-situ observation of the grain growth and grain boundary movement in sintered Cu nanoparticle interconnects, Acta Mater. 236 (2022) 118135, https://doi.org/10.1016/j.actamat.2022.118135.

[11] W. Liu, J. Wang, Y. Gao, L. Ji, J. Zhang, G. Zhang, P. Liu, Simulation, prediction and verification of the thermal and electrical properties of sintered copper joints with random pore structure for power electronics packaging, in: 2024 25th International Conference on Electronic Packaging Technology (ICEPT), 2024, pp. 1–6, https://doi.org/10.1109/ICEPT63120.2024.10668544.

[12] M.-S. Kim, H. Nishikawa, Silver nanoporous sheet for solid-state die attach in power device packaging, Scr. Mater. 92 (2014) 43–46, https://doi.org/10.1016/j.scriptamat.2014.08.010.

[13] X. Wang, Z. Yang, L. Ji, Z. Zeng, H. Chen, J. Fan, J. Zhang, P. Liu, An SEM-based finite element analysis of Cu-Ag sintered joints on thermal shock reliability, in: 2024 25th International Conference on Electronic Packaging Technology (ICEPT), 2024, pp. 1–6, https://doi.org/10.1109/ICEPT63120.2024.10668475.

[14] J. Wang, S. Yodo, H. Tatsumi, H. Nishikawa, Reliability-enhanced microscale Ag sintered joint doped with AlN nanoparticles, Mater. Lett. 349 (2023) 134845, https://doi.org/10.1016/j.matlet.2023.134845.

[15] Y.-J. Kim, B.-H. Park, S.-K. Hyun, H. Nishikawa, The influence of porosity and pore shape on the thermal conductivity of silver sintered joint for die attach, Mater. Today Commun. 29 (2021) 102772, https://doi.org/10.1016/j.mtcomm.2021.102772.

[16] F. Qin, Y. Hu, Y. Dai, T. An, P. Chen, Evaluation of thermal conductivity for sintered silver considering aging effect with microstructure based model, Microelectr. Reliab. 108 (2020) 113633, https://doi.org/10.1016/j.microrel.2020.113633.

[17] H. Zhang, Y. Liu, L. Wang, F. Sun, J. Fan, M.D. Placette, X. Fan, G. Zhang, Effects of sintering pressure on the densification and mechanical properties of Nanosilver double-side sintered power module, IEEE Trans. Compon. Packag. Manuf. Technol. 9 (5) (2019) 963–972, https://doi.org/10.1109/TCPMT.2018.2884032.

[18] W. Lv, J. Liu, X. Lei, F. Zhu, Porosity dependence of thermal and electrical properties in nano-silver paste, IEEe Trans. Electron. Devices 70 (2) (2023) 702–707, https://doi.org/10.1109/TED.2022.3229256.

[19] S.T. Chua, K.S. Siow, Microstructural studies and bonding strength of pressureless sintered nano-silver joints on silver, direct bond copper (DBC) and copper substrates aged at 300°C, J. Alloys. Compd. 687 (2016) 486–498, https://doi.org/10.1016/j.jallcom.2016.06.132.

[20] Y. Yao, Q. Huang, S. Wang, Effects of porosity and pore microstructure on the mechanical behavior of nanoporous silver, Mater. Today Commun. 24 (2020) 101236, https://doi.org/10.1016/j.mtcomm.2020.101236.

[21] M. Wang, N. Pan, Numerical analyses of effective dielectric constant of multiphase microporous media, J. Appl. Phys. 101 (11) (2007), https://doi.org/10.1063/1.2743738.